RSC Advances

PAPER

View Article Online
View Journal | View Issue

Check for updates

Cite this: *RSC Adv.*, 2021, **11**, 3280

Oxidative esterification of renewable furfural on cobalt dispersed on ordered porous nitrogen-doped carbon†

Defeng Yin,[a] Yanxia Zheng,[a] Lixi Yang,[a] Shuyue Li,[a] Daqing Zhu,[a] Yafei Guo,[b] Cuncun Zuo,*[a] Yuchao Li,*[a] Haofei Huang[a] and Ming Wang[a]

A series of highly dispersed cobalt-based catalysts on N-doped ordered porous carbon (Co-NOPC) were synthesized using the sacrificial-template method. MCM-41, ZSM-5 and SBA-15 were employed as hard templates with 2,2′-bipyridine as the ligand. The physical and chemical properties of the Co-NOPC catalyst were characterized by Raman, XRD, SEM, TEM, EDX, ICP, BET, XPS. Co-NOPC had been proven to be a highly efficient catalyst for oxidative esterification of furfural (FUR) to methyl 2-furoate without alkaline additives. Catalytic performance was correlated to the dispersed cobalt, porous structure and specific surface area. The relationship between oxygen activation and the strong interaction of cobalt and pyridine nitrogen were confirmed by XPS. Catalytic performance enhancement mechanisms were correlated with the redistribution of electrons at the interface between carbon material and cobalt atoms through the molecular dynamics method and a reaction mechanism was also proposed. The optimized catalysts showed outstanding catalytic activity and stability and no obvious decrease in activity was found after 6 cycles with 99.6% FUR conversion and 96% methyl 2-furoate selectivity.

Received 24th November 2020
Accepted 30th December 2020

DOI: 10.1039/d0ra09945g

rsc.li/rsc-advances

Open Access Article. Published on 15 January 2021. Downloaded on 2/5/2026 1:14:04 AM.
This article is licensed under a Creative Commons Attribution-NonCommercial 3.0 Unported Licence.

1. Introduction

Renewable biomass resources are promising alternatives for the sustainable supply of chemical intermediates and liquid fuels.[1] The non-precious metal approach for production of chemicals from biomass resources is attracting immense research interest globally, which is very important from the perspectives of green chemistry and sustainable development.[2,3] Furfural (FUR) is one of the most common platform chemicals derived from lignocellulosic biomass, with an annual production volume of more than 200 000 tons.[4] FUR with an aldehyde group and furan ring is an α,β-unsaturated carbonyl compound which can be applied for oxidative esterification,[5] oxidation-condensation,[6] hydrogenation reduction,[7] decarbonization, and reduction amination under certain conditions.[8]

Oxidative esterification of FUR to methyl 2-furoate is an important reaction in the fine chemical industry. Methyl 2-furoate was used to produce alkyl furoates which often were used as fragrance components and flavors.[9] Traditionally, methyl 2-furoate is synthesized by two steps: (i) FUR was oxidized to through strong oxidants such as $KMnO_4$. (ii) Thenfuroic acid was esterified by concentrated H_2SO_4 in methanol.[10–12] However, $KMnO_4$ and H_2SO_4 can corrode the reaction equipment and the yield of product is low and cannot be further improved. Recently, supported noble metals, such as Pd, Ag, Au, and bimetallic catalysts, were synthesized for the oxidative esterification of FUR to methyl 2-furoate with alkaline additives, such as CH_3ONa, K_2CO_3.[13–15] We have prepared a kind of Au-supported cerium oxide doped manganese ($Au/MnCeO_x$) for oxidative esterification of methyl acrolein to methyl methacrylate with highly yield 90.5%.[16] Noble metal catalyst has the advantages of higher activity, higher stability and lower leaching rate, but it suffers excessive price.

More recently, non-noble metal materials have been widely investigated due to its abundant reserves and equivalent catalytic activity with noble metal catalysts. Among these non-noble metal catalysts, highly dispersed ones have attracted the most of attentions due to their maximum atomic utilization and excellent activity. Jagadeesh[17,18] synthesized a cobalt-based nanocatalyst Co_3O_4/NGr@C. The active site consists of Co_3O_4 nanoparticles surrounded by N-doped graphene layer. It exhibited excellent catalytic performance for the activation of molecular oxygen. Han[19] reported a nano-coating N-doped sub-3 nm Co-based nano-particle catalyst, which showed high catalytic efficiency for the oxidative esterification of aldehydes. Porous supports are needed to disperse active metal nano-particles. Zhou[20] employed ZIF-67 as self-template to prepare N-doped porous carbon, which showed high catalytic activity for oxidative esterification of alcohols to esters. Li[21] synthesized an Co-

[a]School of Chemistry and Chemical Engineering, Institute of Clean Chemical Industry, Shandong University of Technology, Zibo 255049, P. R. China
[b]School of Chemical Engineering and Pharmacy, Henan University of Science and Technology, Luoyang 471000, P. R. China

† Electronic supplementary information (ESI) available. See DOI: 10.1039/d0ra09945g

© 2021 The Author(s). Published by the Royal Society of Chemistry

Open Access Article. Published on 15 January 2021. Downloaded on 2/5/2026 1:14:04 AM.
This article is licensed under a Creative Commons Attribution-NonCommercial 3.0 Unported Licence.

based N-doped ordered porous carbon catalyst (ISAS-Co/OPNC) by hard template method with SBA-15 as sacrificial template. The catalyst has high specific surface area, ordered pores and highly dispersed cobalt nano-particles. It suggests that the performance of catalyst is largely determined by the supports. The ideal carrier not only shortens the diffusion pathway but also provides high specific surface area and suitable pores structure.[22,23]

In order to prepare highly efficient non-noble metal catalysts, pore structure of the support has been adjusted to increase the accessibility of the Co–N_x active sites in this work. A series of highly dispersed cobalt-based N-doped on ordered porous carbon catalyst (Co-NOPC) were used for oxidative esterification of FUR to methyl 2-furoate. The catalysts were synthesized by hard template method. The complex of cobalt chloride and 2,2′-bipyridine were filled into the pore channel of sacrifice template (using MCM-41, ZSM-5, SBA-15). Due to the constraint effect of the sacrificial template and the strong coordination effect of the cobalt chloride and 2,2′-bipyridine ligand, highly dispersed cobalt-based N-doped ordered porous carbon material was obtained. The catalysts were characterized *via* XRD, Raman, SEM, TEM, BET, ICP–MS, and XPS. Catalyst activity and the influence of pore structure were investigated and the stability of the catalyst was also tested.

2. Materials and methods

2.1 Chemicals and materials

2,2′-Bipyridine, ethanol, cobalt(II) chloride hexahydrate ($CoCl_2 \cdot 6H_2O$), hexadecyltrimethyl ammonium bromide (CTAB), tetraethyl orthosilicate (TEOS), sodium hydroxide (NaOH), triblock copolymer $EO_{20}PO_{70}EO_{20}$ (P123) and ZSM-5 molecular sieve were purchased from Aladdin. MCM-41 and SBA-15 molecular sieve were self-prepared. All the chemicals are analytical grade and were not purified before use.

2.2 Preparation of the catalysts

The process of preparing Co-NOPC catalyst was reported in literature with slightly change in Fig. 1.[24] Firstly, 5 g the template, 4.68 g of 2,2′-bipyridine were dissolved in 20 ml mixture of water and ethanol (v : v = 1 : 1) under robust stirring at 80 °C. 2.37 g $CoCl_2 \cdot 6H_2O$ were dissolved in 50 ml ethanol. Then the two solutions were mixed to form a yellow solution and kept stirring for 12 h at 80 °C. The solvent was removed at 80 °C overnight. The obtained solid was pyrolyzed at 800 °C with a heating rate of 4 °C min^{-1} under the protection of N_2 in a tube furnace for 2 h. Then the black carbon material was etched in 6 M NaOH solution for 24 h to remove template and bulk Co nano-particles. The material was collected by centrifugation, and washed with warm mixed solution of ethanol and water. Finally, the obtained catalyst was dried at 70 °C under vacuum overnight. Co-NOPC-SBA-15, Co-NOPC-ZSM-5 and Co-NOPC-MCM-41 were abbreviated to Co-NOPC-S, Co-NOPC-Z and Co-NOPC-M, respectively.

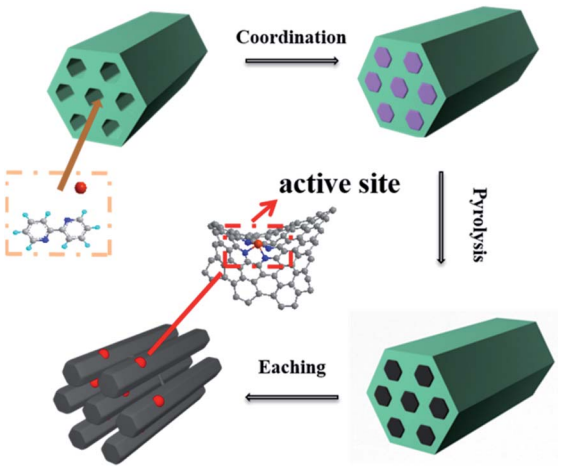

Fig. 1 Preparation process of Co-NOPC catalyst.

2.3 Characterization of the catalyst

Powder X-ray diffraction (XRD) data of supports and catalysts were collected by a Philips PW-1830 X-ray diffractometer with Cu Kα (λ = 1.5406 Å). The wide-angle X-ray diffraction data were collected with a scan speed at 7° min^{-1} from 5° to 80°. The small-angle X-ray diffraction data was analyzed with scan speed at 0.5° min^{-1} from 0.5° to 10°. The Raman spectra were tested on a Raman spectrometer (Lab RAM HR800) which equipped with a CCD detector at 514 nm. The scanning electron microscope (SEM) data was acquired by a Sirion 200 scanning electron microscope with the accelerating voltage at 10 kV. The morphology patterns of Co-NOPC catalyst were collected by a transmission electron microscopy (TEM) with Tecnai G2F20 transmission electron microscope equipped with a Super-X EDS detector. The pore size distribution and surface area were performed by N_2 physical adsorption and desorption (Micromeritics ASAP 2460). The specific surface area and pore size distribution were simulated by BET and BJH method, respectively. X-ray photoelectron spectroscopy (XPS) were collected by a Thermo ESCALAB 250Xi spectrometer with Al Kα radiation (Al Kα = 1846.6 eV) as the excitation source. Inductive coupled plasma (ICP, PerkinElmer ICP-OES 7300DV) measurement was applied to analysis the elemental content of Co-NOPC catalysts. Organic Element Analyzer measurement was applied to analysis the elemental content of Co-NOPC catalysts on an element analyzer (ElementarVario EL cube).

2.4 Procedure for the oxidative esterification

Co-NOPC catalyst (0.5 g), FUR (50 mmol), methanol (500 mmol) were mixed in a 50 ml autoclave at room temperature. The reaction was carried out at 80 °C with magnetic stirring and the autoclave was charged with 0.5 Mpa O_2 with the gas flow at 15 ml min^{-1}. After two hours, the autoclave was rapidly cooled down to room temperature and the O_2 were discharged. Then, the products were quantitative by GC using *n*-heptane as internal standard.

3. Results and discussion

3.1 Materials characterization

In order to explore the crystalline and pore structures of catalysts, XRD was performed. The small-angle XRD patterns of

Open Access Article. Published on 15 January 2021. Downloaded on 2/5/2026 1:14:04 AM.
This article is licensed under a Creative Commons Attribution-NonCommercial 3.0 Unported Licence.

MCM-41 (Fig. S1†) exhibited three peak located at 2.2°, 3.4° and 4.2°, which were assigned to (100), (110), and (200) planes, corresponding to highly ordered MCM-41 type materials with a hexagonal structure.[25] The small-angle XRD pattern of SBA-15 (Fig. S1†) exhibited similar three peaks located at 0.9°, 1.4° and 1.7°, which were assigned to (100), (110) and (200) planes, corresponding to highly ordered SBA-15 type materials with a hexagonal structure.[26] The *d* spacing values were calculated according to the Bragg's law. The obtained α value from different planes for each sample are fairly consistent, confirming the successful formation of the hexagonal structure of SBA-15 and MCM-41 in Table S1.† The average cell parameters were calculated to be 4.1 nm and 9.8 nm for MCM-41 and SBA-15, respectively.

The pattern of Co-NOPC-Z in Fig. 2 showed three peaks at 44.2°, 51.6° and 75.8° which can be corresponded to (111), (200) and (220) planes of metallic Co (JCPDS 15-0806). However, no prominent characteristic peak of metallic Co and oxidative Co were observed in Co-NOPC-S and Co-NOPC-M, indicating the higher dispersion of Co nano-particles than Co-NOPC-Z. It is probably due to the confinement effect of sacrificial-template and the strong coordination effect of Co with 2,2′-bipyridine, which limited the polymerization of Co nano-particles.[27]

Raman spectroscopy was applied to investigate the graphitization degrees of carbon (Fig. 3). All the Raman spectra of Co-NOPC catalysts showed D and G peaks at 1349.6 cm^{-1} and 1593.1 cm^{-1}, respectively.[28] The strength of the D band is related to the structural defects, while G band is corresponding to the in-plane vibrations of the sp^2-C.[29] The calculated I_D/I_G peak area ratio of Co-NOPC-S, Co-NOPC-Z and Co-NOPC-M were 1.06, 1.20 and 1.23, respectively, indicating that Co-NOPC-M has the most of the structural defects and contains amorphous carbon.

SEM and TEM measurements were performed to explore the micro morphology and pore structure of catalysts. TEM images showed that the mesoporous molecular sieve MCM-41 and SBA-15 were synthesized successfully (Fig. S2†). Co-NOPC-S, Co-NOPC-Z and Co-NOPC-M showed the similar lamellar structure (Fig. 4a–c). All these three catalysts showed multilayered

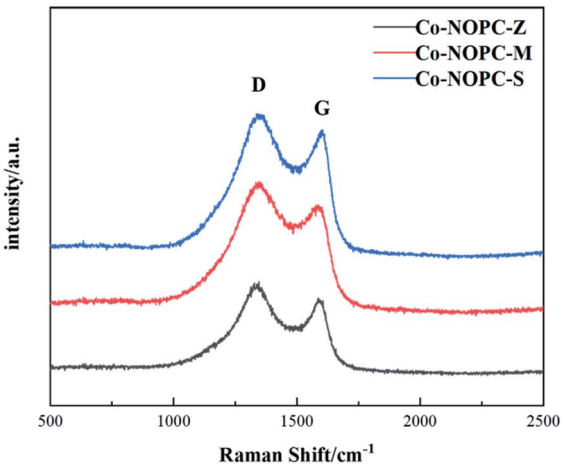

Fig. 3 Raman spectra of Co-NOPC catalysts.

ordered flaky structures. The fragments of Co-NOPC-S and Co-NOPC-M were more dispersed than Co-NOPC-Z. Size of the sheet for Co-NOPC-M is smaller than Co-NOPC-S. The TEM of Co-NOPC-M (Fig. 4d) revealed that it displayed well-defined ordered mesoporous structure, which remained the ordered pore structure of MCM-41 after the etching of hard template.[30] The cobalt particle size of Co-NOPC-M (2.8 ± 0.5 nm) was smaller than that of Co-NOPC-S (3.5 ± 0.7 nm) and Co-NOPC-Z (5.7 ± 1.4 nm) catalysts (Fig. 5). The cobalt particle size of Co-NOPC-M and Co-NOPC-S catalysts were small and relatively concentrated which may due to the differences in the structure of molecular sieves. Furthermore, the EDX mappings of Co-NOPC-M suggested O, N and Co were evenly distributed (Fig. 6).

Element contents of catalysts measured by ICP-OES and Organic Element Analyzer were shown in Table 1. The content of Si for all the samples was lower than 4%, suggesting the efficient etching by NaOH. The contents of Co for Co-NOPC-M, Co-NOPC-S and Co-NOPC-Z were 2.7 wt%, 2.3 wt% and 1.7 wt%, respectively. The Co-NOPC-M also presented the higher content of N (9.2 wt%) than Co-NOPC-S (7.9 wt%) and Co-NOPC-Z (8.3 wt%).

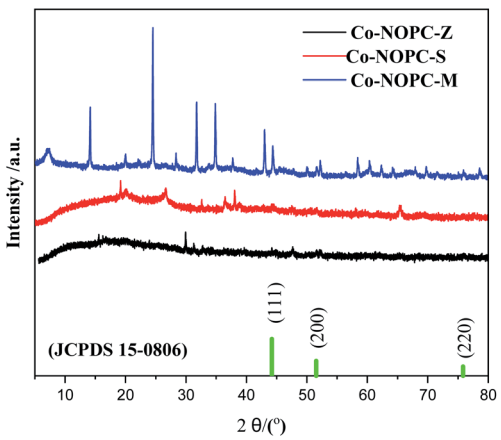

Fig. 2 XRD patterns of catalysts.

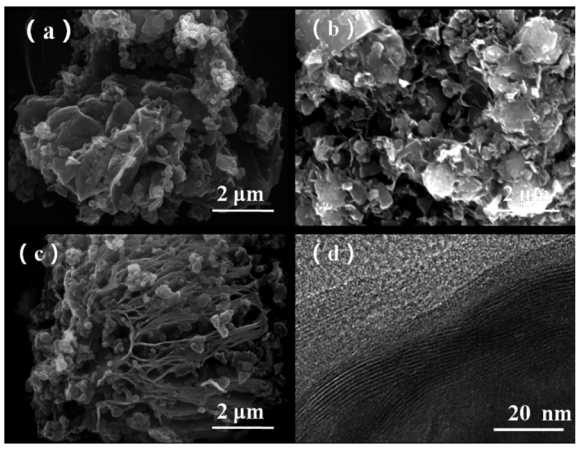

Fig. 4 SEM images of *o*-NOPC-S (a), Co-NOPC-Z, (b) Co-NOPC-M (c), TEM image of Co-NOPC-M (d).

© 2021 The Author(s). Published by the Royal Society of Chemistry

Open Access Article. Published on 15 January 2021. Downloaded on 2/5/2026 1:14:04 AM.
This article is licensed under a Creative Commons Attribution-NonCommercial 3.0 Unported Licence.

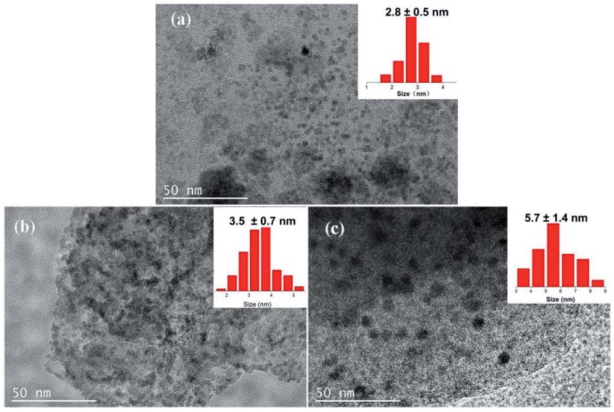

Fig. 5 TEM images and particle size distribution of Co-NOPC-M (a), Co-NOPC-S (b), Co-NOPC-Z (c).

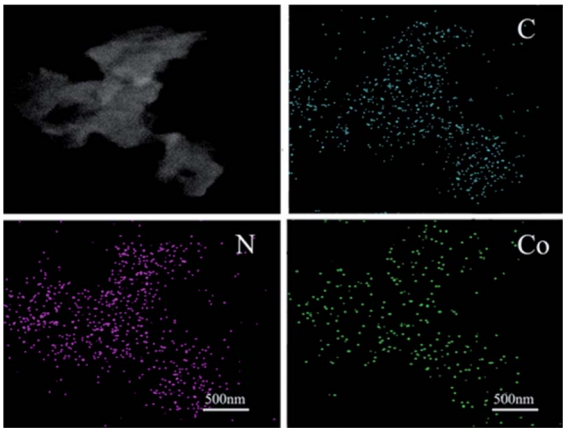

Fig. 6 EDX mappings of N, O and Co of the catalyst Co-NOPC-M.

N_2 adsorption–desorption isotherms measurement was performed to investigate the pore structural. MCM-41 showed the highest BET surface area (860 m^2 g^{-1}) than SBA-15 (567 m^2 g^{-1}) and ZSM-5 (274 m^2 g^{-1}) (Table S2†). The pore wall thickness is defined as the difference between the average unit cell parameter and the pore size (Table S2†). MCM-41 showed a thinner pore wall thickness (1.7 nm) than SBA-15 (7.1 nm), which demonstrates that the Co-NOPC-M catalyst would have smaller pore size than Co-NOPC-S (Table S2†). All the catalysts (Fig. 7a) exhibited H4 hysteresis loop, which indicates a lot of big packing pores generated during the etching process. The BET surface area of Co-NOPC-M, Co-NOPC-S and Co-NOPC-Z were 532 m^2 g^{-1}, 395 m^2 g^{-1} and 258 m^2 g^{-1}, respectively (Fig. 5b). The pore size of catalysts exhibited inverse trend around 1.8 nm, 2.5 nm and 3.4 nm, respectively (Table 1). The different pore size between Co-NOPC-M and Co-NOPC-S was mainly due to the difference of wall thickness and pore size of sacrifice template. The wall of MCM-41 and SBA-15 were removed after etching by 6 M NaOH solution, and then the pore structure of catalysts formed (Fig. 1). The porous and ordered pore structure is crucial for the transport of reactants, products and high surface area is favorable for accessible property of active sites.

XPS was applied to explore the chemical state of Co-NOPC. As expected, all the XPS spectra of prepared catalysts revealed the presence of C, N, Co, Si and O peaks, indicating the co-doping of N and Co on ordered carbon (Fig. S4†). The occurrence of Si peak possibly arises from sacrifice template which was not totally cleaned. The C 1s peaks in Co-NOPC catalysts were fitted into four peaks around 284.4 eV, 285.7 eV, 286.8 eV and 288.8 eV corresponding to sp^3 C–C, C–N & C=N, C–O and O=C–O, respectively (Fig. 6a, d and g).[31,32] The N 1s peaks of Co-NOPC catalysts was deconvoluted into four peaks: pyridinic N, pyrrolic N, graphitic N, and nitric oxide, corresponding to the binding energies at 398.3 eV, 399.1 eV, 400.8 eV and 404.8 eV, respectively (Fig. 8b, e and h).[33] The relative content of pyridinic N (Table 1) was higher in Co-NOPC-M (around 1.24%) than Co-NOPC-S (0.82%) and Co-NOPC-Z (0.43%). The pyridinic N was assigned to the Co–N_x, which is crucial to activate the oxygen to active species.[34,35] In the Co 2p spectrum of Co-NOPC (Fig. 8c, f and i), three catalysts presented similar spectra with the electron binding energy of Co^{2+} $2p_{3/2}$ and Co^{3+} $2p_{1/2}$ locating around 779.3 eV and 796.3 eV, respectively, indicating that Co centers had a higher electron density. These Co centers can be ascribed to the fact that Co particles bonded with N in the graphitic sheets, which agrees with previous research.[36,37] The peaks located at 785.7, 803.3 eV are assigned to be the satellite peaks. The metallic Co species (BE = 777.9 eV) were not detected by XPS for Co-NOPC-M and Co-NOPC-S. Co-NOPC-Z solely unveiled the existence of Co^0 $2p_{3/2}$ band at 778.10 eV, which is agreed well with the XRD results showing a pure metallic Co phase for Co-NOPC-Z. It is most likely due to that the pore size of ZSM-5 is larger and cannot form a strong constraint on cobalt, which leads to the growth of cobalt nanoparticles. Thus, the similar chemical valence state of Co-NOPC

Table 1 Hole structure data and elemental analysis of Co-NOPC catalysts

			Element contents			
Sample	Surface area[a] (m^2 g^{-1})	Pore size[b] (nm)	Co[c] (wt%)	N[d] (wt%)	Si[c] (wt%)	Pyridinic N[e] (wt%)
Co-NOPC-M	532	1.8	2.7	9.2	1.3	1.24
Co-NOPC-S	395	2.5	2.3	7.9	0.3	0.82
Co-NOPC-Z	258	3.4	1.7	8.3	3.6	0.43

[a] Surface area evaluated by using the BET model. [b] Pore size evaluated by using the BJH model. [c] Co and Si content measured by ICP–MS. [d] N content measured by Organic Element Analyzer. [e] Pyridinic N content measured by XPS.

© 2021 The Author(s). Published by the Royal Society of Chemistry

Open Access Article. Published on 15 January 2021. Downloaded on 2/5/2026 1:14:04 AM.
This article is licensed under a Creative Commons Attribution-NonCommercial 3.0 Unported Licence.

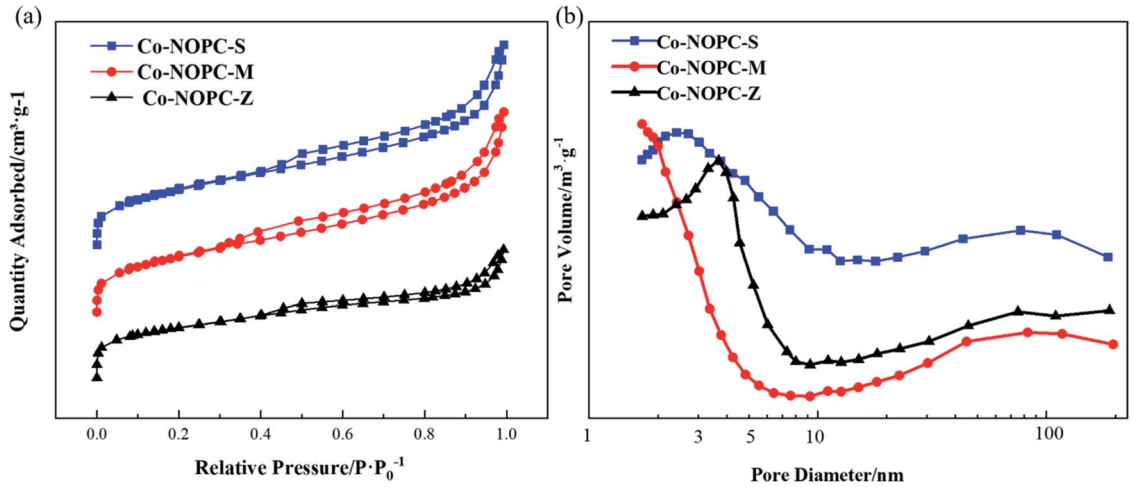

Fig. 7 (a) N_2 adsorption isotherm linear plot of Co-NOPC catalysts, (b) pore size distribution for Co-NOPC catalysts.

catalysts proved that Co and N were doped into the ordered carbon material and formed Co–N_x active sites by the electron transfer of surface Co to electronegative N atoms.[38] The covalent bonds between Co–N and the carbon skeleton not only have synergistic effect, but also improve the structural stability of the Co-NOPC catalyst.

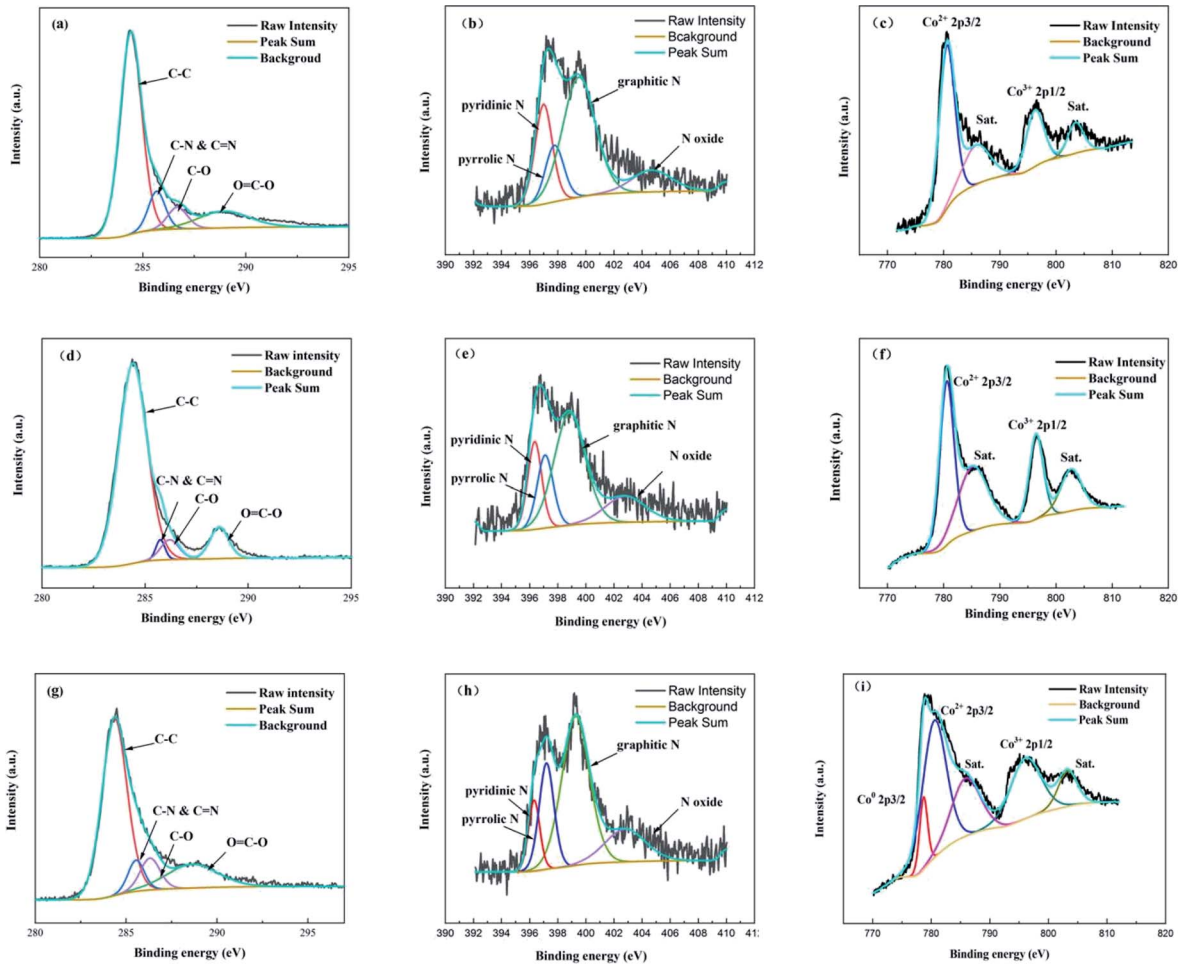

Fig. 8 XPS spectra of Co-NOPC catalysts. High resolution XPS spectra of C 1s (a), N 1s (b) and Co 2p (c) regions for Co-NOPC-M, high resolution XPS spectra of C 1s (d), N 1s (e) and Co 2p (f) regions for Co-NOPC-S and high resolution XPS spectra of C 1s (g), N 1s (h) and Co 2p (i) regions for Co-NOPC-Z.

© 2021 The Author(s). Published by the Royal Society of Chemistry

Open Access Article. Published on 15 January 2021. Downloaded on 2/5/2026 1:14:04 AM.
This article is licensed under a Creative Commons Attribution-NonCommercial 3.0 Unported Licence.

3.2 Catalytic performance

The catalytic performance of Co-NOPC was evaluated for the oxidative esterification of FUR to methyl 2-furoate under mild condition at presence of oxygen without additional base (Fig. 9). No methyl 2-furoate was found without catalysts, which indicates that catalyst plays the key role in the reaction system. The effect of cobalt in catalytic processes was also investigated. NOPC-M was applied for oxidative esterification of FUR only with yield around 0.2%, suggesting that cobalt is the main active sites. The catalytic performance of Co-NOPC-S, Co-NOPC-M, Co-NOPC-Z was also investigated and the results were summarized. Co-NOPC-M showed the highest conversion (99.6%) and methyl-2-furoate selectivity (96%). 65% of FUR with the selectivity of methyl-2-furoate 46.3% were obtained over Co-NOPC-S. Compared to other catalysts, Co-NOPC-Z showed the lowest conversion of FUR (43%), the selectivity of methyl-2-furoate is also poor (38%). The Co-NOPC-M catalyst also showed superior stability. The catalytic performance showed no significant decrease after 6 cycles for oxidative esterification of FUR (Fig. 10).

Analysis of the Co-NOPC structure was further conducted to explain why nitrogen rich carbon support activates the Co nanoparticles for the selective oxidation of furfural. Comparing all three Co-NOPC catalysts prepared, the relative content of pyridinic N and Co and specific surface area are associated with catalytic performance. The relative content of pyridinic N in Co-NOPC catalysts had a direct relationship with the conversion and selectivity of the oxidative esterification (Fig. S7a and b†). As the pyridinic nitrogen content increased, the conversion and selectivity increased correlatively. Meanwhile, the relative content of cobalt content is related to the conversion of furfural, but has a weak correlation with selectivity (Fig. S7c and d†). The pyridinic N and cobalt were the effective sites forming Co–N_x as reported.[38,39] EDX mappings of N, O and Co of the catalyst Co-NOPC-M showed that Co and N had high dispersion. At the same time, XPS data showed that Co mainly existed as Co^{2+} $2p_{3/2}$ and Co^{3+} $2p_{1/2}$, which could prove that the catalyst formed the CO–N_x active site. The electronegativity of doped nitrogen may stabilize deposited metal and increase the binding energy of cobalt–carbon, which would enhance the catalyst stability.[40] At the same time, the doped nitrogen atoms can increase the electron density of the active metal and promote oxidative ability of Co atoms.[41] Co-NOPC-M catalyst has higher content of pyridine nitrogen and Co, which can form more active sites. During the catalyst preparation process, the hard template is removed by 6 M NaOH solution, and the framework of the hard template changes into ordered mesoporous channels. N_2 adsorption–desorption isotherms and TEM revealed that the Co-NOPC-M catalyst had order mesoporous structure with the highest surface area of 532 m^2 g^{-1}. As Fig. S7e and f† revealed, the specific surface area is also closely related to the conversion of oxidative esterification. Meanwhile, the active metal particle size of Co-NOPC-M catalyst is smaller, which is also conducive to improve the activity of the catalyst. High specific surface area, ordered mesoporous structure and smaller particle size are crucial for the transport of reactants and the accessible property of active sites. In summary, the highest activity of Co-NOPC-M catalyst is mainly due to the following advantages: high active site content, high dispersion of active site, high specific surface area, ordered pore structure, and smaller particle size.

The incorporate of nitrogen into NOPC materials could control the electronic structure of cobalt which would reduce valence band and increase conduction band.[42–44] Nitrogen-rich carbon with a relatively higher flat band potential (or work function) than that of metallic Co materials, will accept electrons from Co nano-particles until their Fermi level reaches equilibrium. The Mott–Schottky effect leads to the redistribution of electrons at the interface between carbon material and cobalt atom and more positive charges accumulation in the cobalt atoms.[45] The more oxidative area thus forms on the side of the Co nano-particles accordingly. In addition, the nitrogen atom doped in the electron-rich carbon material can be used as an anchor group to bond with the metal center to form complex centers with homogeneous coordination compounds. And the phenomenon can improve the catalytic performance, make the loaded metal nano-particles more dispersed, avoiding the aggregation of metal particles.[46] In previous research, alkaline additives, such as CH_3ONa, K_2CO_3, were used to speed up the deprotonation process, which is important step to form ester. In

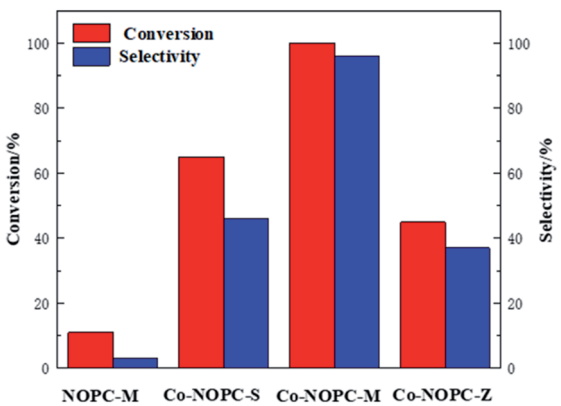

Fig. 9 Oxidative esterification of FUR with Co-NOPC catalysts.

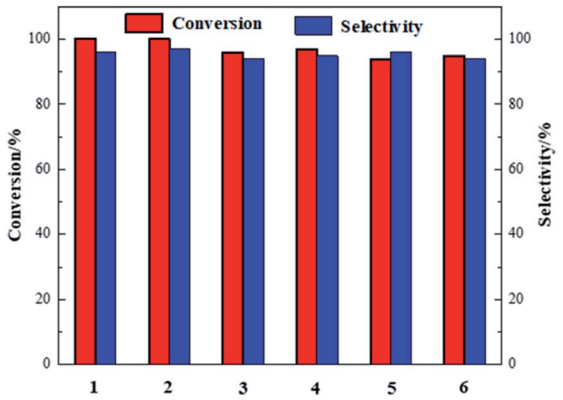

Fig. 10 The recyclability of Co-NOPC-M catalyst for oxidative esterification of FUR.

Open Access Article. Published on 15 January 2021. Downloaded on 2/5/2026 1:14:04 AM.
This article is licensed under a Creative Commons Attribution-NonCommercial 3.0 Unported Licence.

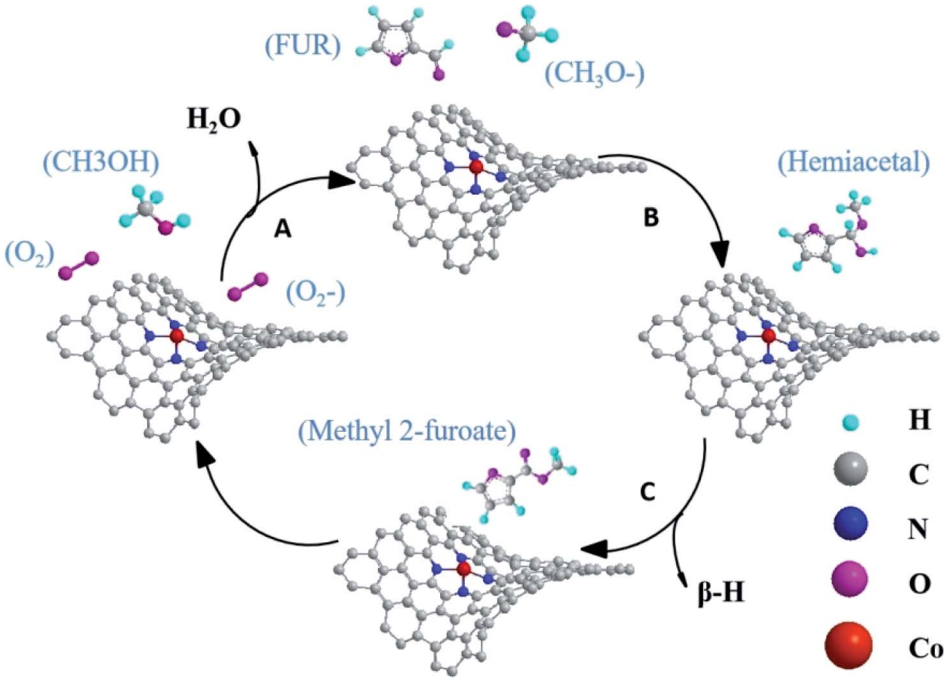

Fig. 11 Reaction mechanism of oxidative esterification on Co-N/PCN catalysts.

this reaction, the electron-poor cobalt has sufficient strength to attract and activate O_2 to eliminate protons from H-cobalt.

Based on the above discussion, the mechanism for oxidative esterification of FUR with methanol to methyl 2-furoate was speculated. As shown in Fig. 11, oxygens were activated to superoxide radical anion at the Co–N_x active sites,[34,45] then reactive oxygen ($^{\bullet}O_2^-$) attacks methanol and converts methanol to methoxy in step A. Then the doped nitrogen atoms continued to absorb substrates. Methoxy reacts with FUR to generate the intermediate hemiacetal in step B. Finally, intermediate hemiacetal remove β-H to generate methyl 2-furoate and H_2O.[16,19,47] These finding will be helpful in the application of Co–N/PCN catalysts for oxidative esterification.

4. Conclusions

A series of highly dispersed cobalt-based N-doped ordered porous carbon was prepared *via* hard template method. The pore structure of the support was adjusted by using different sacrifice templates (SBA-15, MCM-41, ZSM-5), which revealed that hard template has a significant effect on the pore structure and catalytic performance. The Co-NOPC-M catalyst showed the best catalytic performance than the catalysts for the oxidative esterification with high conversion of FUR (99.6%) and selectivity of methyl 2-furoate (96%) under mild condition. The good catalytic performance and recyclable characteristics were due to the highly dispersed cobalt, order mesoporous structure and large specific surface area.

Conflicts of interest

There are no conflicts to declare.

Acknowledgements

This work was supported by the Natural Science Foundation of China (21706149 & 21908132). We would also thank SDUT & Zibo City Integration Development Project (2018ZBXC387) and SDUT & Zhangdian District, Zibo City Integration Development Project (2018).

References

1 C.-H. Zhou, X. Xia, C.-X. Lin, D.-S. Tong and J. Beltramini, *Chem. Soc. Rev.*, 2011, **40**, 5588–5617.
2 N. Huo, H. Ma, X. Wang, T. Wang, G. Wang, T. Wang, L. Hou, J. Gao and J. Xu, *Chin. J. Catal.*, 2017, **38**, 1148–1154.
3 J. Cai, H. Ma, J. Zhang, Z. Du, Y. Huang, J. Gao and J. Xu, *Chin. J. Catal.*, 2014, **35**, 1653–1660.
4 B. Kamm, P. R. Gruber and M. Kamm, *Biorefineries-industrial processes and products*, Wiley-VCH, Weinheim, 2006.
5 H. Zhou, S. Hong, H. Zhang, Y. Chen, H. Xu, X. Wang, Z. Jiang, S. Chen and Y. Liu, *Appl. Catal., B*, 2019, 117767.
6 I. Sádaba, M. Ojeda, R. Mariscal, J. L. G. Fierro and M. L. Granados, *Appl. Catal., B*, 2011, **101**, 638–648.
7 X. Zhang, M. Han, G. Liu, G. Wang, Y. Zhang, H. Zhang and H. Zhao, *Appl. Catal., B*, 2019, **244**, 899–908.
8 J. Q. Li, *Chem. Eng. J.*, 2001, **81**, 338–339.
9 E. Angélica, P. Míriam, S. ángel, G. Mónica, P. Analia, R. Gustavo and B. Guillermo, *J. Coat. Technol. Res.*, 2019, **16**, 159–166.
10 M. Manzoli, F. Menegazzo, M. Signoretto and D. Marchese, *Catalysts*, 2016, **6**, 107.
11 Q.-Y. Zhou, S.-h. Wang and W.-y. Shi, *Chem. Eng.*, 2008, **8**, 57–59.

© 2021 The Author(s). Published by the Royal Society of Chemistry

Open Access Article. Published on 15 January 2021. Downloaded on 2/5/2026 1:14:04 AM.
This article is licensed under a Creative Commons Attribution-NonCommercial 3.0 Unported Licence.

12 R. Radhakrishnan, K. Kannan, S. Kumaravel and S. Thiripuranthagan, *RSC Adv.*, 2016, **6**, 45907–45922.
13 F. Menegazzo, M. Signoretto, F. Pinna, M. Manzoli, V. Aina, G. Cerrato and F. Boccuzzi, *J. Catal.*, 2014, **309**, 241–247.
14 M. Signoretto, F. Menegazzo, L. Contessotto, F. Pinna, M. Manzoli and F. Boccuzzi, *Appl. Catal., B*, 2013, **129**, 287–293.
15 M. J. Taylor, L. J. Durndell, M. A. Isaacs, C. M. Parlett, K. Wilson, A. F. Lee and G. Kyriakou, *Appl. Catal., B*, 2016, **180**, 580–585.
16 Y. Tian, Y. Li, Y. Zheng, M. Wang, C. Zuo, H. Huang, D. Yin, Z. Fu, J. Tan and Z. Zhou, *Ind. Eng. Chem. Res.*, 2019, **58**, 19397–19405.
17 R. V. Jagadeesh, T. Stemmler, A. E. Surkus, M. Bauer and M. Beller, *Nat. Protoc.*, 2015, **10**, 916–926.
18 F. A. Westerhaus, R. V. Jagadeesh, G. Wienhfer, M.-M. Pohl, J. R. Radnik, A.-E. Surkus, J. Rabeah, K. Junge, H. Junge and M. Nielsen, *Nat. Chem.*, 2013, **5**, 537–543.
19 J. Han, F. Gu and Y. Li, *Chem.–Asian J.*, 2016, **11**, 2594–2601.
20 Y.-H. Lu and H.-T. Chen, *J. Phys. Chem. C*, 2014, **118**, 10043–10052.
21 J. Ke, J.-W. Xiao, W. Zhu, H. Liu, R. Si, Y.-W. Zhang and C.-H. Yan, *J. Am. Chem. Soc.*, 2013, **135**, 15191–15200.
22 H. Yunhu, Y.-G. Wang, W. Chen, R. Xu, L. R. Zheng, J. Zhang, J. Luo, R.-A. Shen, Y. Zhu and W.-C. Cheong, *J. Am. Chem. Soc.*, 2017, **139**, 17269–17272.
23 A. Han, W. Chen, S. Zhang, M. Zhang, Y. Han, J. Zhang, S. Ji, L. Zheng, Y. Wang and L. Gu, *Adv. Mater.*, 2018, 1706508.
24 Y. Han, Z. Wang, R. Xu, W. Zhang, W. Chen, L. Zheng, J. Zhang, J. Luo, K. Wu, Y. Zhu, C. Chen, Q. Peng, Q. Liu, P. Hu, D. Wang and Y. Li, *Angew. Chem., Int. Ed.*, 2018, **57**, 11262–11266.
25 A.-M. Brezoiu, M. Deaconu, I. Nicu, E. Vasile, R.-A. Mitran, C. Matei and D. Berger, *Microporous Mesoporous Mater.*, 2019, **275**, 214–222.
26 J. Du, H. Xu, J. Shen, J. Huang, W. Shen and D. Zhao, *Appl. Catal., A*, 2005, **296**, 186–193.
27 L. Zhang, J. Wang, N. Shang, S. Gao, Y. Gao and C. Wang, *Appl. Surf. Sci.*, 2019, **491**, 544–552.
28 M. Li, F. Xu, H. Li and Y. Wang, *Catal. Sci. Technol.*, 2016, **6**, 3670–3693.
29 J. Li, G. Liu, X. Long, G. Gao, J. Wu and F. Li, *J. Catal.*, 2017, **355**, 53–62.
30 S. Molaei, T. Tamoradi, M. Ghadermazi and A. Ghorbani-Choghamarani, *Microporous Mesoporous Mater.*, 2018, S1387181118303585.
31 Z. K. Yang, C.-Z. Yuan and A.-W. Xu, *ACS Energy Lett.*, 2018, **3**, 2383–2389.
32 X. Ma, Y.-X. Zhou, H. Liu, Y. Li and H.-L. Jiang, *Chem. Commun.*, 2016, **52**, 7719–7722.
33 R. V. Jagadeesh, K. Natte, H. Junge and M. Beller, *ACS Catal.*, 2015, **5**, 1526–1529.
34 R. V. Jagadeesh, H. Junge, M.-M. Pohl, J. R. Radnik, A. Brückner and M. Beller, *J. Am. Chem. Soc.*, 2013, **135**, 10776–10782.
35 Y. Pan, G. Wu, Y. He, J. Feng and D. Li, *J. Catal.*, 2019, **369**, 222–232.
36 L. Zhang, A. Wang, W. Wang, Y. Huang, X. Liu, S. Miao, J. Liu and T. Zhang, *ACS Catal.*, 2015, **5**, 6563–6572.
37 T. Zhang, W. Liu, L. Zhang, W. Yan, X. Liu, X. Yang, S. Miao, W. Wang and A. Q. Wang, *Chem. Sci.*, 2016, **10**, 1039.
38 Y. Gao, G. Hu, J. Zhong, Z. Shi, Y. Zhu, D. S. Su, J. Wang, X. Bao and D. Ma, *Angew. Chem., Int. Ed.*, 2013, **52**, 2109–2113.
39 M. Groves, A. Chan, C. Malardier-Jugroot and M. Jugroot, *Chem. Phys. Lett.*, 2009, **481**, 214–219.
40 X. Xu, Y. Li, Y. Gong, P. Zhang, H. Li and Y. Wang, *J. Am. Chem. Soc.*, 2012, **134**, 16987–16990.
41 P. Zhang, Y. Gong, H. Li, Z. Chen and Y. Wang, *Nat. Commun.*, 2013, **4**, 1593.
42 C. Wang, L. Qiao, C. Qu, W. Zheng and Q. Jiang, *J. Phys. Chem. C*, 2011, **113**, 812–818.
43 H. J. Xiang, B. Huang, Z. Y. Li, S.-H. Wei, J. L. Yang and X. G. Gong, *Phys. Rev. X*, 2011, **2**(1), 278–279.
44 X. Wang, X. Li, L. Zhang, Y. Yoon, P. K. Weber, H. Wang, J. Guo and H. Dai, *Science*, 2009, **324**, 768–771.
45 H. Su, K.-X. Zhang, B. Zhang, H.-H. Wang, Q.-Y. Yu, X.-H. Li, M. Antonietti and J.-S. Chen, *J. Am. Chem. Soc.*, 2017, **139**, 811–818.
46 X. H. Li and M. Antonietti, *Chem. Soc. Rev.*, 2014, **44**, 6593–6604.
47 L. Zhang, A. Wang, W. Wang, Y. Huang, X. Liu, S. Miao, J. Liu and T. Zhang, *ACS Catal.*, 2015, **5**, 6563–6572.

© 2021 The Author(s). Published by the Royal Society of Chemistry